Oxygen Reduction Hot Paper

How to cite: *Angew. Chem. Int. Ed.* **2023,** *62,* e202301433
International Edition: doi.org/10.1002/anie.202301433
German Edition: doi.org/10.1002/ange.202301433

Approaching Theoretical Performances of Electrocatalytic Hydrogen Peroxide Generation by Cobalt-Nitrogen Moieties

*Runjia Lin, Liqun Kang, Karolina Lisowska, Weiying He, Siyu Zhao, Shusaku Hayama, Graham J. Hutchings, Dan J. L. Brett, Furio Corà, Ivan P. Parkin, and Guanjie He**

Abstract: Electrocatalytic oxygen reduction reaction (ORR) has been intensively studied for environmentally benign applications. However, insufficient understanding of ORR $2e^-$-pathway mechanism at the atomic level inhibits rational design of catalysts with both high activity and selectivity, causing concerns including catalyst degradation due to Fenton reaction or poor efficiency of H_2O_2 electrosynthesis. Herein we show that the generally accepted ORR electrocatalyst design based on a Sabatier volcano plot argument optimises activity but is unable to account for the $2e^-$-pathway selectivity. Through electrochemical and *operando* spectroscopic studies on a series of CoN_x/carbon nanotube hybrids, a construction-driven approach based on an extended "dynamic active site saturation" model that aims to create the maximum number of $2e^-$ ORR sites by directing the secondary ORR electron transfer towards the $2e^-$ intermediate is proven to be attainable by manipulating O_2 hydrogenation kinetics.

Introduction

Electrochemical oxygen reduction reaction (ORR), in which O_2 is reduced to either OH^-/H_2O by $4e^-$-transfer as required for fuel cell/metal-air battery applications, or through a $2e^-$-pathway to produce green H_2O_2, is critical for global electrification and decarbonisation.[1–4] Holding multiple reaction pathways can be a double-edged sword which raises difficulty in selectivity control.[5] On one hand, many $4e^-$-transfer-dominated catalysts experience serious degradation when peroxide by-product is accumulated and triggers the destructive Fenton reaction; on the other, low selectivity would lead to poor energy efficiency for H_2O_2 generation.[6,7] Pt-based catalysts exhibit excellent $4e^-$ ORR activity and selectivity but are expensive and unstable for mass utilization.[8] Affordable oxygen-functionalized carbons show high $2e^-$-transfer selectivity but sluggish kinetics.[9] Hence, a trade-off among activity, selectivity and cost, restricts the current ORR catalyst design. Transition metal (TM) catalysts are promising candidates for solving the deadlock owing to their tuneable catalytic behaviour and abundance. However, TM-based catalysts suffer from poor stability as fuel cell cathodes or low selectivity when employed for generating H_2O_2 due to insufficient understanding on their $2e^-$-pathway mechanism at the atomic level.[10] Investigating the precise origin of selectivity towards the $2e^-$-pathway is vital not only for boosting H_2O_2 production efficiency, but also to enhance $4e^-$-catalyst durability by avoiding sites responsible for $2e^-$ ORR at the synthesis stage.

Herein, we show that the generally accepted Sabatier volcano plot argument optimises ORR activity but is unable to account for the $2e^-$-pathway selectivity; an extended "dynamic active site saturation" model that examines in addition the hydrogenation kinetics linked to the OOH* adsorption energy enables us to resolve the activity-selectivity compromise. Electrochemical and *operando* spectroscopic studies on the ORR process governed by a series of $Co–N_x$/carbon nanotube hybrids indicate that manipulat-

[*] R. Lin, K. Lisowska, S. Zhao, F. Corà, I. P. Parkin, G. He
Christopher Ingold Laboratory, Department of Chemistry, University College London
20 Gordon Street, London WC1H 0AJ (UK)
E-mail: g.he@ucl.ac.uk

L. Kang, W. He
Department of Inorganic Spectroscopy, Max-Planck-Institute for Chemical Energy Conversion
Stiftstr. 34–36, 45470 Mülheim an der Ruhr (Germany)

L. Kang, S. Zhao, D. J. L. Brett, G. He
Department of Chemical Engineering, University College London (UCL)
London, WC1E 7JE (UK)

S. Hayama
Diamond Light Source Ltd
Diamond House, Harwell Campus, Didcot, OX11 0DE (UK)

W. He
University of Göttingen, Institute of Inorganic Chemistry
Tamannstrasse 4, 37077 Göttingen (Germany)

R. Lin, G. J. Hutchings
Max Planck-Cardiff Centre on the Fundamentals of Heterogeneous Catalysis FUNCAT, Cardiff Catalysis Institute, School of Chemistry, Cardiff University
Cardiff (UK)

G. He
School of Chemistry, University of Lincoln
Brayford Pool, Lincoln LN6 7TS (UK)

ing O_2 hydrogenation kinetics can direct the secondary ORR electron transfer step towards the $2e^-$ intermediate, accordingly maximising the population of the $2e^-$ ORR sites. Control experiments reveal the O_2 hydrogenation chemistry is related to a catalyst reconstruction with lower symmetry around the Co active centre induced by applying cathodic potentials. The optimised catalyst exhibits a $\approx$100% H_2O_2 selectivity and an outstanding activity with a high potential of 0.82 V *versus* the reversible hydrogen electrode to reach the ring current density of 1 mA cm^{-2} by using rotating ring-disk electrode (RRDE) measurement, which is the best-performing $2e^-$ ORR electrocatalyst reported to date, and approaches the thermodynamic limit.

Results and Discussion

Electron transfer to the O_2 molecule, whether directed to the $2e^-$ or $4e^-$ reduction, occurs in multiple elementary steps in which electrons are transferred one at a time. Both $2e^-$ or $4e^-$ reductions initiate with the formation of *OOH intermediates in the first step, and are likely differentiated by whether the second electron transfer leads to the formation of HO_2^- intermediates ($2e^-$-pathway) or dissociation of the O–O bond in the intermediate ($4e^-$-pathway). A selection of data from cutting-edge $2e^-$ ORR electrocatalysts in the recent literature have been collected, on which a statistical analysis has been established to identify possible correlations between atomic features of the active site and selectivity (Figure 1a and Supporting Information Figure S1). Most of the metal-free catalysts (i.e. refs. [11,13,16] in the light green region) tend to exhibit high selectivity but poor kinetic activity while the electrocatalytic behaviour is the other way round for many of the metal-based catalysts (i.e. refs. [19,20,21] in the dark green region), indicating the existence of a compromise between enduing high $2e^-$ reaction activity and selectivity. Interestingly, none of the reported catalysts reaches the thermodynamic limit of $2e^-$ ORR performance (blue star in Figure 1a, more information in Supporting Information Figure S2) despite many of them (dots with pink outer shells in Figure 1a), according to computational studies, claim to approach the Sabatier volcano peak (refers to the optimised OOH* adsorption energy for O_2 to H_2O_2 conversion predicted on the basis of thermodynamic analysis,[11,19] more information in Supporting Information Figure S1b) by either tailoring the active centres directly[11,14] or their coordination environments.[15,19] The notable gap between the observed experimental results and the thermodynamic limit challenges the correctness of the "volcano plot peak worship" catalyst design approach meanwhile demands the study of $2e^-$ ORR from a comprehensive understanding of kinetic processes. We have recently proposed an alternative "dynamic active site saturation" theory[27] according to which it is believed the worse-than-expected $2e^-$ ORR activity can be attributed to the competing $2e^-$ and $4e^-$ reaction pathways (more specifically, the competitions between OOH* desorption and dissociation reactions). A schematic diagram of the possible reaction rate evolution of each electron transfer step during the ORR is given in Figure 1b, where $k_{1\ opt}$ *O_2 and $k_{2\ opt}$ *OOH_{opt} (brown box) represent the O_2* hydrogenation and OOH* desorption rates of a catalyst which complies with the Sabatier principle for the $2e^-$ reaction pathway. When taking the competition between OOH* desorption and dissociation into account (blue box, in which $k_{1\ opt}$ *O_2, $k_{2\ opt}$ *$OOH_{opt\ des}$ and k_3 *$OOH_{opt\ dis}$ represent the rates of O_2* hydrogenation, OOH* desorption and dissociation, respectively), optimised H_2O_2 production will be attained only if the desorption-oriented OOH* (orange dots in Figure 1b) outweighs the dissociation-oriented OOH* (green dots in Figure 1b). Part of the OOH*, Which are required to desorb to maximise H_2O_2 selectivity will instead proceed to the $4e^-$ pathway if the desorption and dissociation steps share comparable rates (which accordingly makes $k_{2\ opt}$ *$OOH_{opt\ des}$ smaller than $k_{2\ opt}$ *OOH_{opt}). The H_2O_2 generation rate will consequently be restricted by the diminished numbers of desorption-oriented OOH* despite the catalyst obeying Sabatier principle. In this case, the $2e^-$

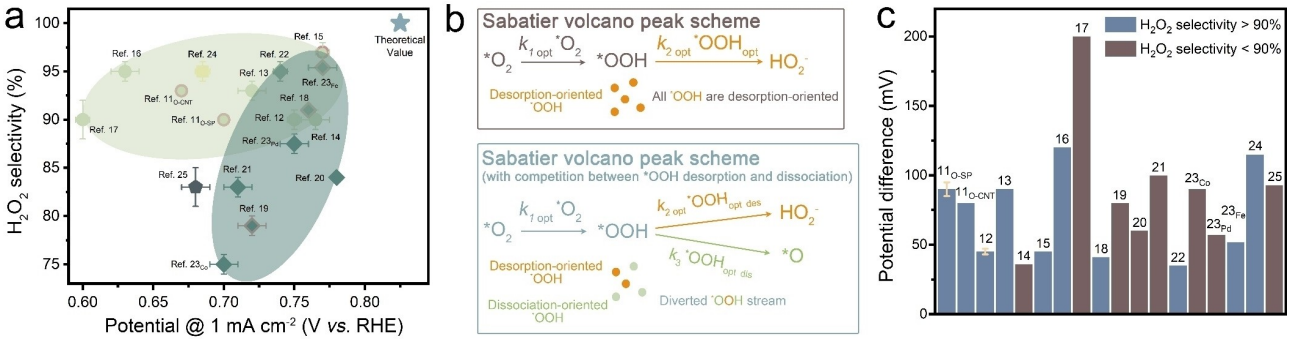

Figure 1. a) Comparison of $E_{@1\ mA\ cm^{-2}}$ (the potential at which ring current density reaches 1 mA cm^{-2}, more discussion in Supporting Information Figure S2) and the corresponding selectivity for H_2O_2 electrosynthesis in recently reported state-of-the-art electrocatalysts (in alkaline medium, examined by RRDE system, more information available in Supporting Information Table S1).[11–25] b) Thermodynamic and kinetic analysis of $2e^-$-ORR process based on the well-accepted Sabatier volcano peak theory and the ΔG_{OOH}* deviation model proposed in this work (assuming the reaction rate of each elementary step is determined by the reaction rate constant (k) and the population of specific intermediate.[26] c) Comparison of $\Delta E_{@1\ mA\ cm^{-2}}$ (the potential difference between $E_{@1\ mA\ cm^{-2}}$ and E_{onset}) on the electrocatalysts displayed in (a).

ORR is neither limited by the hydrogenation of O_2 nor desorption of OOH*, but the competition between the desorption and dissociation of OOH*. This provides credible explanation to the excellent onset (due to the optimal O_2 hydrogenation and OOH* desorption) but unsatisfactory $E_{@1\ mA\ cm^{-2}}$ (due to the limited number of OOH* that are prone to be desorbed) of some reported $2e^-$ ORR catalysts (i.e. refs. [17,21,25] in Figure 1c, more discussion available in Supporting Information Note 1). Considering ORR is mass-transfer rather than kinetics limited, avoiding performance saturation by boosting active site population is not predicted to be as effective as it was for the kinetics-limited electrocatalytic system in ref. [27]. In other words, saturation of ORR active site can be prevented, should the OOH* desorption/dissociation competition be optimized. It is considered that the OOH* desorption/dissociation competition can be tuned by regulation of ΔG_{OOH}* (i.e. alterations in O_2* hydrogenation rate could potentially lead to a higher population of desorption-oriented OOH* in Figure 1b blue box scheme, accordingly increasing the rate of OOH* to HO_2^- conversion despite a possible inferior reaction rate constant due to ΔG_{OOH}* deviation, more discussion available in Supporting Information Note 1). Though the deviation in ΔG_{OOH}* from the optimal Sabatier value would sacrifice the performance of onset potentials, an improved $E_{@1\ mA\ cm^{-2}}$ will still be attainable if the benefit from the enlarged population of desorption-oriented OOH* outweighs the reduced kinetic activity. This opens up an exciting opportunity to synergise activity and selectivity by an improved rational design concept for the electrocatalyst.

To explore this possibility, a series of CoN_x/annealed carbon nanotube hybrids (denoted as CoN_{4+4}-ACNT, CoN_4-ACNT and CoN_{2+x}-ACNT) with different Co and N coordination environments were synthesised by heterogenization of different molecular CoN_x complexes onto CNTs via van der Waals force and hydrogen bonding (more information available in Supporting Information Methodology section). Though the use of cobalt-based molecular catalyst in ORR can be traced back to 1964[28] and they have been intensively studied afterwards in terms of onset potential and current density comparison,[29,30] understanding of the correlation between reaction selectivity-atomic coordination is still limited and demands comprehensive investigation. Scanning transmission electron microscopy (STEM) was used to investigate the morphological information of the CoN_x-ACNTs. The CNT framework, which provides mechanical/electron-conductive support for metal active sites, can be identified in the upper panel of Figures 2a–c. The monodispersed bright dots (highlighted in pink circles) in the high-angle annular dark-field (HAADF) STEM images (Figures 2a–c lower panel and Supporting Information Figure S3) indicate the presence of isolated cobalt species in CoN_x-ACNTs.

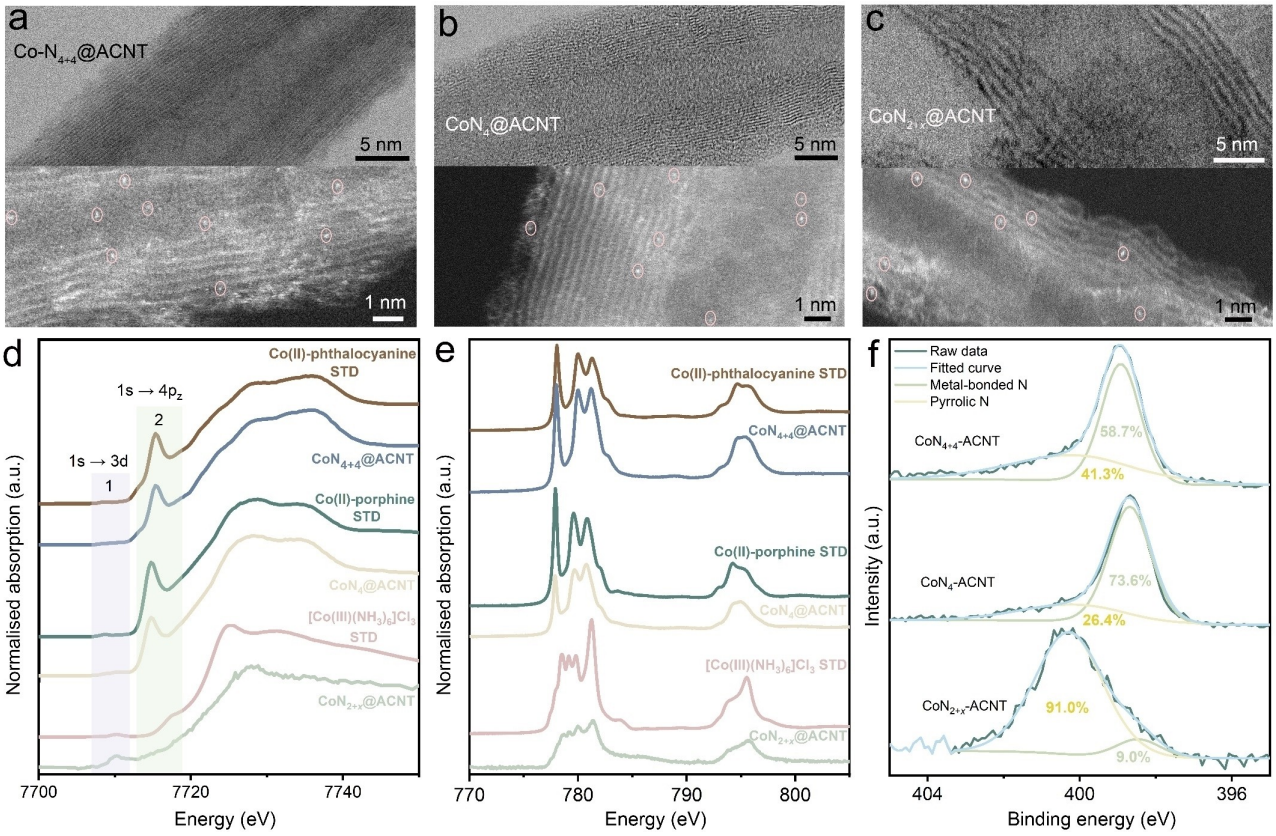

Figure 2. TEM (upper panel) and HAADF-TEM (lower panel) images of a) CoN_{4+4}-ACNT, b) CoN_4-ACNT and c) CoN_{2+x}-ACNT. d) Co K-edge HERFD-XANES, e) Co L_3-edge NEXAFS and f) XPS N 1s spectra of CoN_x-ACNT and reference samples.

To understand physical and chemical properties of as-prepared electrocatalysts, ex situ X-ray absorption spectroscopy (XAS) and X-ray photoelectron spectroscopy (XPS) measurements were performed. The high energy resolution fluorescence detected X-ray absorption near edge structure (HERFD-XANES) spectra (Figure 2d, the corresponding first derivative plot is shown in Supporting Information Figure S4) are characterised by two regions: the weak pre-edge peaks at 7708–7712 eV (labelled as transition region 1) and the strong edge peaks at 7714–7716 eV (labelled as transition region 2). The Co K-edge spectra for CoN_{4+4}-ACNT and CoN_4-ACNT are nearly identical to their Co^{II}-phthalocyanine and Co^{II}-porphine precursors respectively (indicating the molecular structure of the precursors were well-preserved during the heterogenization process), except the slightly weaker second transitions (7714.7 eV for CoN_{4+4}-ACNT and 7715.3 eV for CoN_4-ACNT) due to ACNT encapsulation.[31] The peaks in transition region 1 can be attributed to dipole forbidden 1s to 3d quadrupole transition.[32] The peaks in transition region 2 which have usually been observed in Co–N_4 structures with square planar environment,[32,33] can be assigned to a shake down feature that involves 1s to $4p_z$ transition mixed with a 3d character due to a simultaneous ligand to metal charge transfer. As for the CoN_{2+x}-ACNT sample, its absorption edge position witnesses a $\approx$1 eV shift to a higher energy state compared to CoN_{4+4}-ACNT and CoN_4-ACNT. Through referencing to XANES of the low spin Co^{3+} in $[Co(NH_3)_6]Cl_3$, the CoN_{2+x}-ACNT catalyst is dominated by low spin octahedral Co^{3+} centres. Similar conclusion can also be reached from Co K_β X-ray emission spectroscopy (XES) measurement as Supporting Information Figure S5 demonstrates. The surface atomic structure was investigated through near edge X-ray absorption fine structure (NEXAFS) measurements. As illustrated in Figure 2e, no significant shift of the Co L_3-edge NEXAFS characteristic peaks of CoN_{4+4}-ACNT, CoN_4-ACNT and CoN_{2+x}-ACNT can be observed when compared to their corresponding reference samples. The XPS analysis (Supporting Information Figure S6a) agrees with the NEXAFS measurement that the cobalt centres in CoN_{2+x}-ACNT show higher oxidation states compared to the Co atoms in CoN_{4+4}-ACNT/CoN_4-ACNT. The XPS N 1s spectra (Figure 2f) of all CoN_x-ACNT samples display two main peaks corresponding to pyrrolic N ($\approx$400.5 eV) and metal-bonded N ($\approx$399 eV).[34] The CoN_{4+4}-ACNT contains a higher proportion of surface N atoms which are not directly bonded to the Co centres (41.3 at%) compared to that of CoN_4-CNT (26.4 at%), consistent with the molecular structure. Extended X-ray absorption fine structure (EXAFS) studies confirm the coordination environment of CoN_{4+4}-ACNT is in good agreement with that of Co phthalocyanine, which is featured with 4 direct coordinated N atoms and additional N atoms in the second coordination shell (Supporting Information Figures S7). Although CoN_{2+x}-ACNT is estimated (from the NEXAFS measurement) to exhibit the highest coordination number of the central metal among the three materials, XPS N 1s spectrum indicates most of its N species (91 at %) are not directly bonded with the central Co. Computational simulation studies in literatures suggest the Co centres in metal-pyrrole structure are possibly bonded with two pyrrolic N and surrounded with N atoms in polypyrrole chains (whose formation is likely due to the polymerisation of the pyrrole precursor).[35] The stronger Co K-edge pre-edge peak in HERFD-XANES of CoN_{2+x}-ACNT compared to that of $[Co(NH_3)_6]Cl_3$ could be a fingerprint of the Co being in a lower symmetry (i.e. non-centrosymmetric) environment when coordinated to polypyrrole chains relative to the square planar porphyrin coordination.[36] XPS O 1s (Supporting Information Figure S6b) and O K-edge NEXAFS (Supporting Information Figure S10) analysis suggest all three catalysts, despite showing minor differences in spectroscopic responses, share similar O species which mainly come from the ACNT substrates.

The physical/chemical results shown above illustrate two important features of all as-prepared CoN_x-ACNT catalysts. First, Co species are in single-atom state. Second, in CoN_4-CNT, the central Co^{2+} is bridged by four N atoms; in CoN_{4+4}-CNT, Co^{2+} centre is surrounded by not only first-shell, but also second-shell N atoms; as for CoN_{2+x}-CNT, its Co is in 3 + oxidation state and directly bonded with two pyrrolic N. The Co–N_2 moieties are surrounded and influenced by a protein-like tertiary structure made of polypyrrole chains.

Measured in 0.1 M KOH aqueous solution using a rotating ring-disk electrode system (RRDE, more experimental set-up details available in in Supporting Information Methodology section), as can be reflected from Figure 3a and b, the CoN_x-ACNT materials with different Co–N coordination environments show similar ORR onset ($\approx$0.86 V vs. RHE) but greatly varied selectivity, with a $\approx$100% H_2O_2 production Faraday efficiency (denoted as $FE_{H_2O_2}$) and a $\approx$2 electron transfer number (denoted as n) for CoN_{4+4}-ACNT in a wide-potential region ranging from $\approx$0.50–0.85 V vs. RHE; mixed selectivity for CoN_4-ACNT and high $4e^-$-pathway selectivity ($FE_{H_2O_2} < 10\%$) for CoN_{2+x}-ACNT. A similar selectivity trend can be observed when the tests are performed in a neutral medium (Supporting Information Figure S11). The performance of CoN_{4+4}-ACNT ($E_{onset} = 0.857$ V vs. RHE, $E_{@1\ mA\ cm^{-2}} = 0.82$ V vs. RHE in 0.1 M KOH) surpasses all previously reported electrocatalysts for H_2O_2 electrosynthesis at both low and high H_2O_2 generation rate conditions and nearly reaches the thermodynamic limit (Figure 3c and Supporting Information Figure S12), indicating the successful solution of the "activity-selectivity dilemma" that puzzles the current $2e^-$ ORR electrocatalysts design. Bulk H_2O_2 electrosynthesis test was also performed with a H-type cell configuration whose results agree with the RRDE measurement (Supporting Information Figure S13), indicating CoN_{4+4}-ACNT can be a promising candidate as a cathode catalyst for H_2O_2 production.

To highlight the superiority of CoN_{4+4}-ACNT over other ORR electrocatalysts, oxygen-functionalized CNT (denoted as OCNT), boron and nitrogen co-doped carbon (denoted as BNC), and oxidized CoN_4-ACNT (denoted as xOCoN_4-ACNT) that represent three popular $2e^-$ ORR electrocatalyst design strategies were synthesised, examined and compared (Figures 3d, e and Supporting Information Fig-

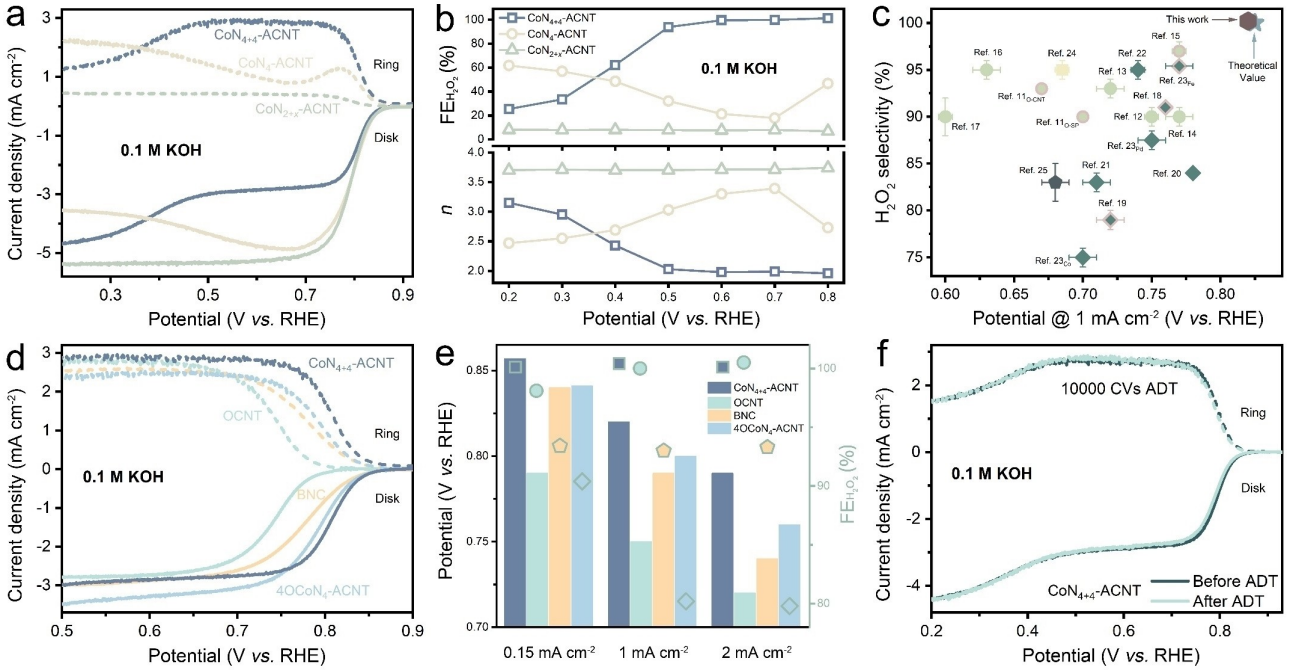

Figure 3. a) Comparison of ORR performance of the CoN_x-ACNT catalysts at 1600 rpm and their simultaneous H_2O_2 detection current densities at the ring electrode in O_2-saturated 0.1 M KOH; b) calculated Faraday efficiency towards H_2O_2 ($FE_{H_2O_2}$) and average number of electrons transferred to each O_2 molecule (*n*) as a function of the applied potential. c) Comparison of the $E_{@1\ mA\ cm^{-2}}$ and selectivity for H_2O_2 electrosynthesis on CoN_{4+4}-ACNT and previously reported electrocatalysts in alkaline medium examined by RRDE system. Comparison of d) ORR polarization curves and e) activity (columns) and selectivity (dots) for CoN_{4+4}-ACNT and other prepared catalysts that represent the current $2e^-$ catalyst design mainstream. f) ADT measurement of CoN_{4+4}-ACNT. More electrochemical data is available in Supporting Information Table S4–S16.

ure S14).[11,19,25] Consistent with previous reports, carbons that are functionalized by oxygen groups exhibit enhanced $2e^-$ ORR behaviour.[11,12,37] The ≈100% $FE_{H_2O_2}$ of OCNT (Supporting Information Figure S14a) confirms the effectiveness of the "O-functionalization" strategy. However, OCNT shows relatively poor activity, requiring 67, 70 and 72 mV higher overpotentials for reaching ring current densities of 0.15, 1 and 2 mA cm^{-2}, respectively compared with that of CoN_{4+4}-ACNT (Figure 3e and Supporting Information Figure S14c). Many attempts were made to manufacture more active $2e^-$ ORR catalysts by heteroatom doping including nitrogen,[24,38] boron,[25,39] and sulfur.[22] Nevertheless, as confirmed in Figure 3e and Supporting Information Figures S14a and c, BNC demonstrates inferior reaction kinetics compared to CoN_{4+4}-ACNT, particularly at high H_2O_2 generation rate (it requires 30 and 50 mV higher overpotentials to reach ring current densities of 1 and 2 mA cm^{-2} and >10% $FE_{H_2O_2}$ decrease compared to that of CoN_{4+4}-ACNT) despite its excellent onset potential (only 17 mV higher overpotential than that of CoN_{4+4}-ACNT). To address the poor activity of metal-free $2e^-$ electrocatalysts, many efforts have been devoted to convert traditional TM-based $4e^-$ ORR electrocatalysts to $2e^-$ structures by tailoring the active centres and/or their surrounding environment.[7,10,21,29,40] The most well-known approach is the oxidation treatment.[41] Therefore, CoN_4 moieties (whose composites with ACNT show mixed ORR selectivity as indicated in Figure 3b) were treated with HNO_3 and then its (refers to the HNO_3-treated CoN_4) hybrid with ACNT was employed as an ORR electrocatalyst (Supporting Information Figure S15). The performance of *x*OCoN_4-ACNT materials demonstrate a strong dependence on the acid treatment duration (selectivity increases but activity decreases with the extension of acid treatment period) as can be seen in Supporting Information Figures S15a and b. In agreement with the conclusion reached in Figure 1a,[10,11,41] there is a competition between activity and selectivity; the modified materials demonstrate better kinetic activities than metal-free ones but unsatisfactory selectivity ($FE_{H_2O_2}$ < 90%). As a result, none of the HNO_3-treated catalysts, even the best performing one (4 h of HNO_3 treatment, denoted as 4OCoN_4-ACNT), displays competitive H_2O_2 production activity compared to CoN_{4+4}-ACNT. The decreasing ring and disk current densities obtained at the same overpotential by prolonged HNO_3 treatment (Supporting Information Figures S15d–f) demonstrate that the improvement in $FE_{H_2O_2}$ is achieved mainly by blocking the $4e^-$ ORR pathway reaction chain rather than by boosting the $2e^-$ ORR pathway kinetics. This result highlights the intrinsic activity/selectivity compromise associated with the strategy of electrocatalyst optimisation through a volcano plot argument based on a destruction-driven approach (i.e. by eliminating non-$2e^-$ ORR sites).[19–21,41] Our dynamic active site saturation model, instead, is a construction-driven approach that aims to create the maximum number of $2e^-$ ORR sites by directing the secondary ORR electron transfer step towards the $2e^-$ intermediate. For further clarification, equivalent current density analysis (named as ECD) is

performed. Results presented in Supporting Information Figure S16c identify reduced overall ORR activities of CoN_4-ACNT after oxidation treatments. That is to say, the ORR process governed by the xOCoN_4-ACNT series (especially 24OCoN_4-ACNT) is restrained by either insufficient numbers of active sites (as implied by the metal loading quantification results displayed in Supporting Information Table S3, uncontrollable harsh oxidation treatment could eradicate part of the pristine metal active sites) or at least one sluggish rate-determining step within its $2/4\,e^-$ reaction chains (due to low activities of the modified active species). The ECD values of CoN_x-ACNT series catalysts are also evaluated (Supporting Information Figure S16b). Their almost identical ECDs suggest the ECD of a catalyst should be close to the $4\,e^-$ ORR mass transfer limitation if it shows full kinetic activity regardless of its selectivity. Hence, research should focus on not only selectivity and onset potential, but also ECD to represent the actual activity when evaluating $2\,e^-$ ORR electrocatalysts.

The catalyst durability has been investigated through accelerated degradation test (ADT) analysis, demonstrated in Figure 3f. The ORR linear sweep voltammetry (LSV) of CoN_{4+4}-ACNT remains almost identical after 10000 cycles of ADT operation. No $FE_{H_2O_2}$ change can be witnessed (Supporting Information Figure S17) which confirms the superb stability of CoN_{4+4}-ACNT for H_2O_2 electrosynthesis. The desirable durability might be attributed to the rigid and very stable Co–N moieties that prevent leaching of cobalt ions (which can behave as an ignitor for Fenton reactions) into the electrolyte.[19] Previous literature suggests disruptive radicals (i.e. OH·) can also be generated via photo/electrocatalytic reduction of H_2O_2.[42] No reduction current can be observed for CoN_{4+4}-ACNT (in high-potential region) during H_2O_2 reduction reaction (H_2O_2RR) tests (Supporting Information Figure S18), inferring the supressed H_2O_2RR activity of CoN_{4+4}-ACNT and the suppression in the production of destructive radicals.

To elucidate the varied selectivity of the CoN_x-ACNT catalysts, control experiments were conducted and indicated the selectivity variation is irrelevant to neither the interaction between the CoN_x complexes and the oxygen-containing carbon substrate nor the metal loading (Supporting Information Figures S19–S22). Attention is then directed to the cobalt-nitrogen coordination where the three catalysts display the biggest difference. To correlate atomic-level coordination with ORR selectivity, *operando* HERFD-XANES Co K-edge measurement was performed (further information on the experiment setup is available in Supporting Information Figure S23). Acquiring XANES in HERFD mode leads to an enhanced spectral resolution, thus expanding the *operando* study of electrocatalysts beyond valence state observation to coordination environment analysis.[43] However, the price for the higher energy resolution to resolve the subtle changes is the difficulties in the measurement because the signal intensity of HERFD-XANES is generally more than one order of magnitude weaker than that of the conventional total fluorescence yield (TFY)/partial fluorescence yield (PFY)-XANES.[44] Hence, HERFD-XANES normally shows lower signal-to-noise ratio (as can be noticed in this work and previous literatures)[44] but the technique is considered reliable (please see Supporting Information Note 2 for more clarifications). The *operando* measurement was first established on CoN_{4+4}-ACNT and CoN_4-ACNT owing to their similar Co coordination chemistry but varied selectivity. The study on CoN_{2+x}-ACNT (Supporting Information Figure S24) will be discussed in a later section. As the applied voltage moves from open circuit voltage (OCP) to 0.61 and 0.26 V vs. RHE, no obvious edge position shift can be noticed in the 1s to 3d transition region (7708–7712 eV, containing information about structural symmetry and oxidation state[32]) nor in the 1s to $4p_z$ transition region (7714–7716 eV, reflecting the charge transfer from ligand to metal[45]). This indicates the oxidation state of Co in both samples remains stable (and indirectly excludes the adsorption of charged ions on Co). A small intensity alteration for both peaks can be observed as a function of applied voltage (Figures 4a and b); even if small (this may reflect the fact that only a small fraction of the Co sites are modified), the intensity change is reproducible in repeated experiments. Variations in the 1s to 3d transition intensity can be assigned to a change of symmetry around the Co ions upon application of a cathodic bias, such as a movement of Co off the molecular plane to a non-centrosymmetric position or adsorption of reaction intermediates on the Co centre, resulting in formation of a penta-coordinated structure which subsequently increases the 1s to 3d transition intensity.[31,36] The Co displacement can also cause p and d type orbital hybridisation, accordingly leading to a decrease in 1s to $4p_z$ transition intensity.[31] In other words, the catalysts witnessed reconstruction in their coordination environment (more in-depth computational analysis on the Co displacement phenomenon is available in Supporting Information Figure S25). Different intensity alterations are observed for 1s to 3d or $4p_z$ transitions on CoN_{4+4}-ACNT and CoN_4-ACNT: referenced to the OCP condition, CoN_4-ACNT shows a larger 1s to $4p_z$ transition intensity change at 0.61 V than at 0.26 V vs. RHE, while the changes in 1s to 3d transition intensity are the other way around. This observation may imply the geometry evolution (from planar to penta-coordinated) is induced by multiple factors, for instance Co displacement and adsorption of ORR intermediates on the Co centre. Considering the hydrogenation of $*O_2$ is normally regarded as the most thermodynamically unfavourable ORR step, the accumulated intermediate could be $*O_2$[21,22] (more discussions in Supporting Information Note 3).

In the case of CoN_4-ACNT, upon decreasing cathodic bias (from 0.61 to 0.26 V vs. RHE) the sample shows a weakening 1s to 3d transition (lower-right inset in Figure 4b). We interpret this change as smaller accumulation of $*O_2$ and hence a more favourable $*O_2$ hydrogenation kinetics at the lower bias. Such observation points to a positive correlation between hydrogenation of $*O_2$ and $2\,e^-$-ORR selectivity, that is, a more favourable $*O_2$ hydrogenation kinetics could lead to better OOH* desorption selectivity. This gives reasons to the increased ORR $2\,e^-$ selectivity of CoN_4-ACNT from 0.7 to 0.2 V vs. RHE

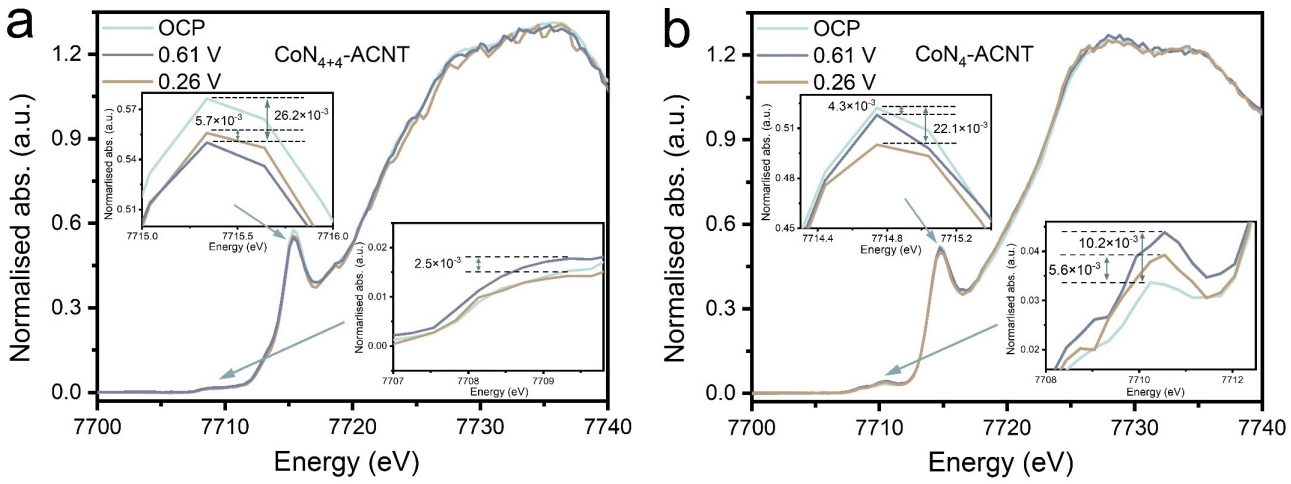

Figure 4. *Operando* HERFD-XANES Co K-edge spectra of a) CoN_{4+4}-ACNT and b) CoN_4-ACNT acquired under chronoamperometry test at OCP, 0.61 and 0.26 V vs. RHE.

(Figure 3a). As for CoN_{4+4}-ACNT, when the potential is set at 0.61 V vs. RHE, the 1s to 3d transition intensity growth (referenced to the OCP condition) of CoN_{4+4}-ACNT is much less than that of CoN_4-ACNT (lower-right insets in Figures 4a and b). This indicates less accumulation of $*O_2$, accordingly pointing to more favourable $*O_2$ hydrogenation kinetics on the prior catalysts. As a result, CoN_{4+4}-ACNT shows higher $2e^-$-ORR selectivity than CoN_4-ACNT. The above analysis validates the hypothesis that the OOH* desorption/dissociation competition can be tuned by adjusting the $*O_2$ hydrogenation kinetics as proposed in Figure 1b. It is noteworthy that the relationship between $*O_2$ hydrogenation and OOH* desorption could vary by active site. In the following work, more comprehensive computational studies (especially from reaction dynamic perspective) are required to provide a better understanding on the positive $*O_2$ hydrogenation-OOH* desorption correlation of the molecular catalysts.

The similar $2e^-$-ORR onset-potential of CoN_{4+4}-ACNT and CoN_4-ACNT (Figure 3a) implies the identical $*O_2$ hydrogenation kinetics of the two catalysts at small overpotentials. To elucidate the reasons behind the varied $*O_2$ hydrogenation kinetics of CoN_{4+4}-ACNT and CoN_{4+4}-ACNT at larger overpotentials, attention is then directed to the 1s to $4p_z$ transition. When biased at 0.61 V vs. RHE, CoN_{4+4}-ACNT witnesses a more obvious 1s to $4p_z$ feature intensity fall (referenced to the OCP condition) compared to that of CoN_4-ACNT (upper-left insets in Figures 4a and b), which implies more active "Co centre wandering" phenomena in CoN_{4+4}-ACNT. This can be ascribed to the second-shell N in CoN_{4+4}-ACNT that facilitates the ligand to metal charge transfer between the first-shell N and the Co centre (more discussion in Supporting Information Note 4). Interestingly, as can be inferred from Figures 4a and b, the larger the 1s to $4p_z$ transition intensity decrease, the smaller the 1s to 3d transition intensity increase (except the CoN_{4+4}-ACNT at 0.26 V which will be described in the following section). This can be regarded as a direct evidence of the positive relationship between the "Co centre wandering" activity and O_2 hydrogenation kinetics. In other words, $\Delta G_{OOH}*$ can be controlled by manipulating the ligand to metal charge transfer chemistry. In summary, CoN_{4+4}-ACNT and CoN_4-ACNT will witness a "Co wandering" coordination reconstruction if cathodically biased (evidencing by the decrease in 1s to $4p_z$ transition). Such reconstruction induces orbital hybridisations of the Co–N_x complexes, owing to which the $*O_2$ hydrogenation kinetics of the catalysts is altered (evidencing by the variation in 1s to 3d transition intensity), eventually resulting in the shift of the OOH* desorption/dissociation competition selectivity. With above discussions, the electrochemical analysis displayed in Figure 3 and the spectroscopic observation shown in Figure 4 are consistent with the hypothesis proposed in Figure 1.

Not only can our analysis be applied to optimise the combined activity and selectivity of the $2e^-$ ORR, but also to better understand open issues in the $4e^-$ ORR operation. Second shell N in Co supported on N-doped carbons (Co–N_x–C) as fuel cell cathodes has been identified as a promoter of H_2O_2 formation that lowers the fuel cell efficiency,[46] but cannot be avoided during practical synthesis especially for cathodes fabricated by high-temperature pyrolysis. In our study, second-shell N is present in the CoN_{4+4} moieties, and we observe a significant suppression in H_2O_2 production (decrease in $FE_{H_2O_2}$) at low-potential (Figures 3 and 5a upper panel). A similar H_2O_2 formation suppression would be highly beneficial in fuel cells and its mechanistic origin warrants further investigation. A control experiment under N_2 atmosphere shows additional redox features in the cyclic voltammetry (CV) plot, centred at ≈0.35V vs. RHE (Figure 5a lower panel). The occurrence of this peak coincides with the onset of $4e^-$ ORR (Figure 5a upper panel and Figure 3b). This indicates that the ORR selectivity variation in CoN_{4+4}-ACNT can occur when the catalyst is able to further accept additional electrons. Despite the noticeable redox pair, no obvious edge position

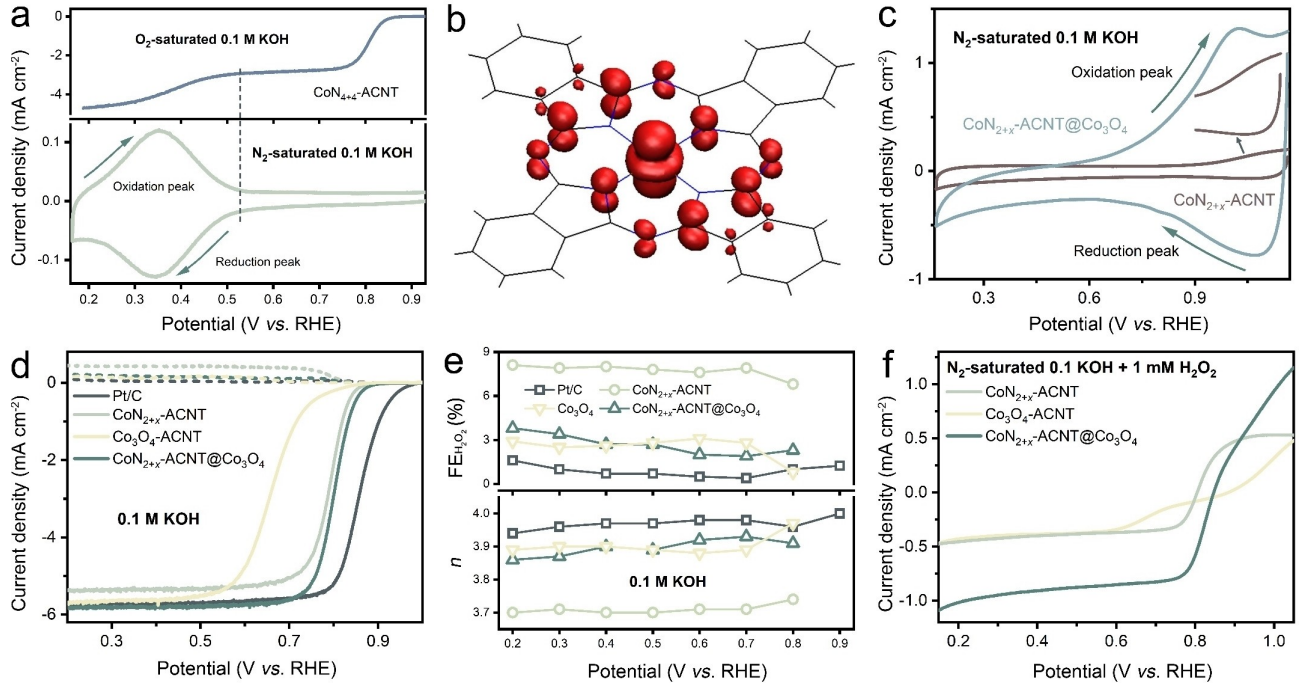

Figure 5. a) ORR polarisation curve (upper panel, measured in O_2-saturated 0.1 M KOH at 1600 rpm) and pseudocapacitive behaviour (lower panel, measured in N_2-saturated 0.1 M KOH at a scan rate of 20 mV s^{-1}) of CoN_{4+4}-ACNT. b) Spin density plot (highlighted in red) of reduced CoN_{4+4}-ACNT from DFT calculations; one unpaired electron is located in the $3d_{z^2}$ orbital of Co^{2+}, and one delocalised over the porphyrin ring. c) Pseudocapacitive behaviour of CoN_{2+x}-ACNT before and after Co_3O_4 hybridisation (scan rate: 20 mV s^{-1}). d), e) Comparison of ORR performance of CoN_{2+x}-ACNT, Co_3O_4-ACNT, CoN_{2+x}-ACNT@Co_3O_4 and Pt/C at 1600 rpm and the simultaneous H_2O_2 detection current densities at the ring electrode in O_2-saturated 0.1 M KOH and (b) the calculated $FE_{H_2O_2}$ and *n* as a function of the applied potential. f) H_2O_2RR polarisation curves of CoN_{2+x}-ACNT, Co_3O_4-ACNT and CoN_{2+x}-ACNT@Co_3O_4 measured in N_2-saturated 0.1 M KOH containing 1 mM H_2O_2 at 1600 rpm. More electrochemical data is available in Supporting Information Table S18–S22.

shift occurs in the Co K-edge HERFD-XANES spectra (Figure 4a), which indicates Co centres are not the major electron acceptors. Computational studies using density functional theory (DFT) reveal that the additional electron in the reduced CoN_{4+4} moieties is localised on the surrounding N atoms instead of the metal centres (Figure 5b and Supporting Information Note 4 for more discussion). By comparison, the CoN_4 molecule without second shell N is more difficult to reduce than CoN_{4+4} (by 1.1 eV in vacuum) and localises the additional electron on the Co centre. Compared to the electrons regulated by the Co centre, electrons on second-shell N may result in the catalytic behaviour change of the reduced CoN_{4+4}-ACNT that promotes the O_2 hydrogenation. This result also infers that the weak Co-K-edge HERFD-XANES pre-edge at 0.26 V vs. RHE in Figure 4a can be attributed to the reduction of the porphyrin ring (which can be seen as another factor besides the "Co wandering" phenomena that influences the O_2* hydrogenation kinetics). Similar to CoN_{4+4}-ACNT, CoN_{6+x}-ACNT shows an obvious redox behaviour (Figure 5c) in a region of potential above 0.9 V vs. RHE, but limited Co edge position shift (only 0.3 eV to lower energy at 0.26 V when referenced to OCP) during the *operando* measurement (Supporting Information Figure S24), suggesting a similar redox mechanism induced by the three-dimensional polypyrrole chains which surround the Co centres and behave as "pseudo-second shell N" electron acceptors.

Inspired by the above results, Co_3O_4 was introduced into the CoN_{2+x}-ACNT system (denoted as CoN_{2+x}-ACNT@Co_3O_4, more characterisation and discussion available in Supporting Information Figures S27 and S30) as a redox behaviour booster (Figure 5c) for more efficient and flexible in situ electron delocalisation. Measured in O_2-saturated 0.1 M KOH (Figures 5d, e and Supporting Information Figure S31), the CoN_{2+x}-ACNT@Co_3O_4 shows ultra-low $FE_{H_2O_2}$ (≈3%) which is only one third of CoN_{2+x}-ACNT (≈9%) and comparable to commercial Pt/C catalyst (≈2%). A similar selectivity enhancement towards the 4e⁻ ORR can also be observed on CoN_{4+4}-ACNT and CoN_4-ACNT after Co_3O_4 hybridisation (Supporting Information Figures S28–S31). Although enhancing 4e⁻ ORR performance by hybridising Co–N_x–C with cobalt oxides has been reported previously,[47,48] the exact origin of the synergy mechanism is still unclear. The selectivity shift was first attributed to the average contribution from the two active centres (i.e. CoN_x and Co_3O_4). That is to say Co_3O_4 should be able to show comparable ORR kinetic activity but more 4e⁻ ORR dominated selectivity than CoN_x moieties, changing the overall reaction selectivity. Nevertheless, as Supporting Information Figures S31a, d and g display, the selectivity shift of CoN_x-ACNT@Co_3O_4 materials can be witnessed prior to the ORR onset/half-wave potential of the Co_3O_4-ACNT catalyst. The almost identical ECD before and after Co_3O_4 hybridisation (Supporting Information Figures S31c, f

and i) also disproves a contribution by Co_3O_4 alone. The diminished H_2O_2 generation after hybridisation could be due to the in situ reduction of the CoN_x-generated H_2O_2 by Co_3O_4. However, the assumption was ruled out by the inadequate H_2O_2RR activity of Co_3O_4-ACNT (Figure 5f). Interestingly, the impact of Co_3O_4 hybridisation on the catalytic behaviour of the CoN_x-ACNT samples is only reflected by ORR selectivity, leaving the activity almost unchanged as implied by the ECD analysis (Supporting Information Figures S30c, f and i). In other words, the catalysts with and without Co_3O_4 share the same rate-limiting step (i.e. hydrogenation of O_2) and reaction kinetics, but the relative contribution of the desorption and dissociation of OOH* varies. This points to the possibility that Co_3O_4 does not directly involve in the initial reduction of O_2 (otherwise an alteration in ORR reaction kinetics should be observed), but can regulate the catalytic process. Combining the discoveries on CoN_{4+4} and the high-potential redox feature of CoN_x-ACNT@Co_3O_4 (redox reaction occurs at a potential higher than the ORR onset potential as can be inferred in Figure 5c), herein, the remaining possibility is proposed that the redox-active Co_3O_4 and the N-rich electron acceptor structures (i.e. tertiary polypyrrole chains, pyrrole N π system) firstly induce an electron delocalisation phenomenon; the delocalised charge then participates in the ORR process on the nearby CoN_x active sites and shifts the reaction selectivity (i.e. by making $\Delta G_O* < \Delta G_{HO_2^-}$ to facilitate the dissociation of OOH*). Such conclusion was supported by a more moderate $FE_{H_2O_2}$ drop of CoN_{4+4}-ACNT@Co_3O_4 compared to that of CoN_{4+4}-ACNT in its redox active potential window (Supporting Information Figure S31e). In other words, the Co_3O_4 advances (evidencing by the decreased H_2O_2 selectivity between 0.5–0.8 V vs. RHE) but does not enhance (evidencing by a similar H_2O_2 selectivity at 0.2 V vs. RHE) the redox-induced electron delocalisation mechanism observed in the CoN_{4+4}-ACNT ORR system. A weakened pseudocapacitive behaviour along with a rebound in $FE_{H_2O_2}$ can be observed for CoN_{2+x}-ACNT@Co_3O_4 after ADT measurement (Supporting Information Figure S32) which further validates the above explanation.

Conclusion

In summary, this work firstly identified the limitations of the popular Sabatier principle-driven $2e^-$ ORR electrocatalyst design, owing to which current ORR electrocatalysts are restricted by activity-selectivity compromise. A "dynamic active site saturation" model was then predicted to synergise the activity and selectivity of the $2e^-$ ORR electrocatalysts. A series of CoN_x-ACNT materials were designed and manufactured to correlate ORR selectivity with Co–N atomic coordination and evaluate the possibility of boosting both activity and selectivity simultaneously. The CoN_{4+4}-ACNT material exhibits a ≈100% $FE_{H_2O_2}$and a high $E_{@1\ mA\ cm^{-2}}$ which is the best-performing $2e^-$ ORR electrocatalyst reported to date, and approaches the theoretical thermodynamic limit. ECD analysis suggests manipulation of selectivity is attainable without sacrificing activity. Through *operando* spectroscopic studies, the excellent $2e^-$ ORR activity and selectivity can be attributed to the optimised O_2 hydrogenation kinetics of the CoN_{4+4} active centre, validating the as-proposed hypothesis. Finally, a redox-induced electron delocalisation mechanism was identified via analysing the pseudocapacitive and ORR behaviours of the CoN_{4+4}-ACNT and CoN_{2+x}-ACNT samples. Such a mechanism was then applied for regulating the H_2O_2 formation of $4e^-$ ORR catalysts. The above discoveries provide fresh insights for electrocatalyst design in both fuel cell and H_2O_2 generation applications.

Acknowledgements

R. Lin would like to thank the University College London for UCL Graduate Research Scholarships and UCL Overseas Research Scholarships. The authors acknowledge Engineering and Physical Sciences Research Council (EP/V027433/1; EP/L015862/1), and Royal Academy of Engineering under the Senior Research Fellowships scheme (Brett) for funding support. We acknowledge the I20 beamline (session ID SP29254), E01 and E02 beamline (session ID MG29207) of electron Physics Science Imaging Centre (ePSIC) in Diamond Light Source (DLS) for the allocated experiment sessions.

Conflict of Interest

There is no conflicts of interests to declare.

Keywords: Cobalt-Nitrogen Moieties · Electrocatalyst · Hydrogen Peroxide · Oxygen Reduction Reaction

[1] M. Kuang, Q. Wang, P. Han, G. Zheng, *Adv. Energy Mater.* **2017**, *7*, 1700193.
[2] Z. Jiang, W. Sun, H. Shang, W. Chen, T. Sun, H. Li, J. Dong, J. Zhou, Z. Li, Y. Wang, R. Cao, R. Sarangi, Z. Yang, D. Wang, J. Zhang, Y. Li, *Energy Environ. Sci.* **2019**, *12*, 3508–3514.
[3] T. Chung Hoon, A. Cullen David, D. Higgins, T. Sneed Brian, F. Holby Edward, L. More Karren, P. Zelenay, *Science* **2017**, *357*, 479–484.
[4] A. Abdelhafiz, A. Vitale, P. Buntin, B. deGlee, C. Joiner, A. Robertson, E. M. Vogel, J. Warner, F. M. Alamgir, *Energy Environ. Sci.* **2018**, *11*, 1610–1616.
[5] P. Peng, L. Shi, F. Huo, C. Mi, X. Wu, S. Zhang, Z. Xiang, *Sci. Adv.* **2019**, *5*, eaaw2322.
[6] A. Zitolo, V. Goellner, V. Armel, M.-T. Sougrati, T. Mineva, L. Stievano, E. Fonda, F. Jaouen, *Nat. Mater.* **2015**, *14*, 937–942.
[7] Y. L. Wang, S. Gurses, N. Felvey, A. Boubnov, S. S. Mao, C. X. Kronawitter, *ACS Catal.* **2019**, *9*, 8453–8463.
[8] Z. Qiao, S. Hwang, X. Li, C. Wang, W. Samarakoon, S. Karakalos, D. Li, M. Chen, Y. He, M. Wang, Z. Liu, G. Wang, H. Zhou, Z. Feng, D. Su, J. S. Spendelow, G. Wu, *Energy Environ. Sci.* **2019**, *12*, 2830–2841.
[9] C. Xia, Y. Xia, P. Zhu, L. Fan, H. Wang, *Science* **2019**, *366*, 226–231.

[10] Y. Wang, R. Shi, L. Shang, G. I. N. Waterhouse, J. Zhao, Q. Zhang, L. Gu, T. Zhang, *Angew. Chem. Int. Ed.* **2020**, *59*, 13057–13062.
[11] Z. Lu, G. Chen, S. Siahrostami, Z. Chen, K. Liu, J. Xie, L. Liao, T. Wu, D. Lin, Y. Liu, T. F. Jaramillo, J. K. Nørskov, Y. Cui, *Nat. Catal.* **2018**, *1*, 156–162.
[12] J. S. Lim, J. H. Kim, J. Woo, D. S. Baek, K. Ihm, T. J. Shin, Y. J. Sa, S. H. Joo, *Chem* **2021**, *7*, 3114–3130.
[13] Y. J. Sa, J. H. Kim, S. H. Joo, *Angew. Chem. Int. Ed.* **2019**, *58*, 1100–1105.
[14] K.-H. Wu, D. Wang, X. Lu, X. Zhang, Z. Xie, Y. Liu, B.-J. Su, J.-M. Chen, D.-S. Su, W. Qi, S. Guo, *Chem* **2020**, *6*, 1443–1458.
[15] G.-F. Han, F. Li, W. Zou, M. Karamad, J.-P. Jeon, S.-W. Kim, S.-J. Kim, Y. Bu, Z. Fu, Y. Lu, S. Siahrostami, J.-B. Baek, *Nat. Commun.* **2020**, *11*, 2209.
[16] H.-X. Zhang, S.-C. Yang, Y.-L. Wang, J.-C. Xi, J.-C. Huang, J.-F. Li, P. Chen, R. Jia, *Electrochim. Acta* **2019**, *308*, 74–82.
[17] Y.-L. Wang, S.-S. Li, X.-H. Yang, G.-Y. Xu, Z.-C. Zhu, P. Chen, S.-Q. Li, *J. Mater. Chem. A* **2019**, *7*, 21329–21337.
[18] H. Gong, Z. Wei, Z. Gong, J. Liu, G. Ye, M. Yan, J. Dong, C. Allen, J. Liu, K. Huang, R. Liu, G. He, S. Zhao, H. Fei, *Adv. Funct. Mater.* **2021**, *31*, 2106886.
[19] E. Jung, H. Shin, B.-H. Lee, V. Efremov, S. Lee, H. S. Lee, J. Kim, W. Hooch Antink, S. Park, K.-S. Lee, S.-P. Cho, J. S. Yoo, Y.-E. Sung, T. Hyeon, *Nat. Mater.* **2020**, *19*, 436–442.
[20] B.-Q. Li, C.-X. Zhao, J.-N. Liu, Q. Zhang, *Adv. Mater.* **2019**, *31*, 1808173.
[21] X. Li, S. Tang, S. Dou, H. J. Fan, T. S. Choksi, X. Wang, *Adv. Mater.* **2021**, *33*, 2104891.
[22] C. Tang, Y. Jiao, B. Shi, J.-N. Liu, Z. Xie, X. Chen, Q. Zhang, S.-Z. Qiao, *Angew. Chem. Int. Ed.* **2020**, *59*, 9171–9176.
[23] K. Jiang, S. Back, A. J. Akey, C. Xia, Y. Hu, W. Liang, D. Schaak, E. Stavitski, J. K. Nørskov, S. Siahrostami, H. Wang, *Nat. Commun.* **2019**, *10*, 3997.
[24] L. Li, C. Tang, Y. Zheng, B. Xia, X. Zhou, H. Xu, S.-Z. Qiao, *Adv. Energy Mater.* **2020**, *10*, 2000789.
[25] Y. Xia, X. Zhao, C. Xia, Z.-Y. Wu, P. Zhu, J. Y. Kim, X. Bai, G. Gao, Y. Hu, J. Zhong, Y. Liu, H. Wang, *Nat. Commun.* **2021**, *12*, 4225.
[26] Z. Hong, S. S. Vasu, D. F. Davidson, R. K. Hanson, *J. Phys. Chem. A* **2010**, *114*, 5520–5525.
[27] R. Lin, L. Kang, T. Zhao, J. Feng, V. Celorrio, G. Zhang, G. Cibin, A. Kucernak, D. J. L. Brett, F. Corà, I. P. Parkin, G. He, *Energy Environ. Sci.* **2022**, *15*, 2386–2396.
[28] R. Jasinski, *Nature* **1964**, *201*, 1212–1213.
[29] B. Lv, X. Li, K. Guo, J. Ma, Y. Wang, H. Lei, F. Wang, X. Jin, Q. Zhang, W. Zhang, R. Long, Y. Xiong, U.-P. Apfel, R. Cao, *Angew. Chem. Int. Ed.* **2021**, *60*, 12742–12746.
[30] Y. Ma, J. Li, X. Liao, W. Luo, W. Huang, J. Meng, Q. Chen, S. Xi, R. Yu, Y. Zhao, L. Zhou, L. Mai, *Adv. Funct. Mater.* **2020**, *30*, 2005000.
[31] J. C. Swarbrick, T.-C. Weng, K. Schulte, A. N. Khlobystov, P. Glatzel, *Phys. Chem. Chem. Phys.* **2010**, *12*, 9693–9699.
[32] M. C. M. Alves, J. P. Dodelet, D. Guay, M. Ladouceur, G. Tourillon, *J. Phys. Chem.* **1992**, *96*, 10898–10905.
[33] H. Peisert, I. Biswas, U. Aygül, A. Vollmer, T. Chassé, *Chem. Phys. Lett.* **2010**, *493*, 126–129.
[34] K. Müller, M. Richter, D. Friedrich, I. Paloumpa, U. I. Kramm, D. Schmeißer, *Solid State Ionics* **2012**, *216*, 78–82.
[35] A. G. Saputro, F. Rusydi, H. Kasai, H. K. Dipojono, *J. Phys. Soc. Jpn.* **2012**, *81*, 034703.
[36] N. Ramaswamy, U. Tylus, Q. Jia, S. Mukerjee, *J. Am. Chem. Soc.* **2013**, *135*, 15443–15449.
[37] L. Han, Y. Sun, S. Li, C. Cheng, C. E. Halbig, P. Feicht, J. L. Hübner, P. Strasser, S. Eigler, *ACS Catal.* **2019**, *9*, 1283–1288.
[38] Y. Sun, I. Sinev, W. Ju, A. Bergmann, S. Dresp, S. Kühl, C. Spöri, H. Schmies, H. Wang, D. Bernsmeier, B. Paul, R. Schmack, R. Kraehnert, B. Roldan Cuenya, P. Strasser, *ACS Catal.* **2018**, *8*, 2844–2856.
[39] D. Iglesias, A. Giuliani, M. Melchionna, S. Marchesan, A. Criado, L. Nasi, M. Bevilacqua, C. Tavagnacco, F. Vizza, M. Prato, P. Fornasiero, *Chem* **2018**, *4*, 106–123.
[40] Q. Zhao, Y. Wang, W.-H. Lai, F. Xiao, Y. Lyu, C. Liao, M. Shao, *Energy Environ. Sci.* **2021**, *14*, 5444–5456.
[41] Q. Zhang, X. Tan, N. M. Bedford, Z. Han, L. Thomsen, S. Smith, R. Amal, X. Lu, *Nat. Commun.* **2020**, *11*, 4181.
[42] T. Hayashi, K. Nakamura, T. Suzuki, N. Saito, Y. Murakami, *Chem. Phys. Lett.* **2020**, *739*, 136958.
[43] M. Agote-Arán, I. Lezcano-González, A. G. Greenaway, S. Hayama, S. Díaz-Moreno, A. B. Kroner, A. M. Beale, *Appl. Catal. A* **2019**, *570*, 283–291.
[44] G. Giannakakis, P. Kress, K. Duanmu, H. T. Ngan, G. Yan, A. S. Hoffman, Z. Qi, A. Trimpalis, L. Annamalai, M. Ouyang, J. Liu, N. Eagan, J. Biener, D. Sokaras, M. Flytzani-Stephanopoulos, S. R. Bare, P. Sautet, E. C. H. Sykes, *J. Am. Chem. Soc.* **2021**, *143*, 21567–21579.
[45] B. Mei, C. Liu, J. Li, S. Gu, X. Du, S. Lu, F. Song, W. Xu, Z. Jiang, *J. Energy Chem.* **2022**, *64*, 1–7.
[46] Z. Miao, Y. Xia, J. Liang, L. Xie, S. Chen, S. Li, H.-L. Wang, S. Hu, J. Han, Q. Li, *Small* **2021**, *17*, 2100735.
[47] N.-F. Yu, C. Wu, W. Huang, Y.-H. Chen, D.-Q. Ruan, K.-L. Bao, H. Chen, Y. Zhang, Y. Zhu, Q.-H. Huang, W.-H. Lai, Y.-X. Wang, H.-G. Liao, S.-G. Sun, Y.-P. Wu, J. Wang, *Nano Energy* **2020**, *77*, 105200.
[48] Y. Tan, W. Zhu, Z. Zhang, W. Wu, R. Chen, S. Mu, H. Lv, N. Cheng, *Nano Energy* **2021**, *83*, 105813.

Manuscript received: January 29, 2023
Accepted manuscript online: March 22, 2023
Version of record online: April 18, 2023